# Automated, unbiased optoretinography reveals comprehensive nanoscopic dynamics of the outer retina in rodents

**Bingyao Tan**[a,b,c,1], **Huakun Li**[b,1], **Veluchamy Amutha Barathi**[c,d,e], **Leopold Schmetterer**[a,b,c,d,f,g,h,i,✉], **and Tong Ling**[a,b,c,✉]

[a]SERI-NTU Advanced Ocular Engineering (STANCE) Program, Singapore
[b]School of Chemistry, Chemical Engineering and Biotechnology, Nanyang Technological University, Singapore
[c]Singapore Eye Research Institute, Singapore National Eye Centre, Singapore
[d]Department of Ophthalmology, Yong Loo Lin School of Medicine, National University of Singapore and National University Health System, Singapore
[e]Academic Clinical Program in Ophthalmology, Duke-NUS Graduate Medical School, Singapore
[f]Department of Ophthalmology, Lee Kong Chian School of Medicine, Nanyang Technological University, Singapore
[g]Department of Clinical Pharmacology, Medical University of Vienna, Austria
[h]Center for Medical Physics and Biomedical Engineering, Medical University of Vienna, Austria
[i]Institute of Molecular and Clinical Ophthalmology, Basel, Switzerland
[1]These authors contributed equally to this work

**Small animals, such as rodents, serve as an attractive option for investigating the intrinsic process of photoreceptor degeneration because of their wide availability and versatility in disease models and gene manipulations. However, there was a lack of an objective and quantitative approach to measure their outer retina dynamics while preserving spatial heterogeneity. Here, we demonstrate an automated, unbiased approach for functional retinal imaging in rodents based on unsupervised machine learning. Our method automatically searches for and classifies nanoscopic cellular dynamics from obscure speckle patterns captured by a low-cost, phase-sensitive optical coherence tomography. Using this approach, we revealed highly reproducible Type-I and Type-II signals in rodents related to different parts of the outer retina. The fast Type-I signal was not reported previously and we hypothesized that it originated from the movement of rod outer segments. We also characterized the light-induced response of the outer retina under scotopic and photopic conditions, and demonstrated *en-face* mapping of the outer retina function in an extended field of view (12°), analogous to multifocal electroretinograms, but only with a single shot and yielding much higher spatial resolution. Our approach can be widely applied to investigating tissue-specific retinal dynamics across animal models, as well as facilitating clinical translations for the early detection of neurodegenerative diseases.**

**optoretinography | unsupervised learning | functional imaging | optical coherence tomography | ocular imaging | rodent**

**Correspondence:** ***leopold.schmetterer@seri.com.sg, tong.ling@ntu.edu.sg***

## Introduction

Optoretinography (ORG) is an optical imaging modality for the non-invasive evaluation of photoreceptor function *in-vivo*. It usually utilizes optical coherence tomography (OCT) to measure function-associated mechanical deformations of specialized neurons in the retina (1–3). A few pilot studies have exploited the ORG to classify cone subtypes according to their responses to chromatic flashes (4) and demonstrated its clinical potential in assessing retinitis pigmentosa (5). Compared with conventional approaches such as electroretinography and visual field testing, ORG is strongly desired in clinical settings owing to its merits in non-invasiveness, objectiveness, and unprecedented spatial resolution. It may serve as an ideal tool for the diagnosis/prognosis of retinal degenerative diseases at the early stage, when no clear signs of degeneration are visible in the structure.

However, several obstacles still hinder ORG from being a clinically ready technology. Photoreceptors are small in diameter, and previous ORG studies on human subjects primarily focused on cone photoreceptors in regions slightly eccentric to the fovea (2, 6, 7). These cones are larger and more sparsely distributed compared with cones in the fovea, and they can be individually resolved by OCT systems equipped with hardware-based (8, 9) or computational adaptive optics (10). Cones in the fovea, whose dysfunction is the hallmark of ocular diseases like age-related macular degeneration, are more difficult to be resolved on an OCT. Additionally, other vision complications, such as age-related cataracts or high refractive errors, particularly among elderly patients, may further complicate the capacity of resolving individual photoreceptors for ORG imaging.

Given the similarity of photoreceptors' structure and function, small animals such as rodents are efficient and cost-effective alternatives for studying the mechanism of photoreceptor degeneration and optimizing experiment protocols for preclinical trials. Rodent retina has a high portion of rods in their photoreceptors (with the ratio being $\sim$97% in mice (11)) and retinal degenerative disease models in rodents are beneficial for studying the early rod degeneration, which often starts prior to the cone degeneration in human retinal degenerative diseases (12–14). Genetically modified animals, such as Gnat1 and Gnat2 mutants and knockout animals, can provide new perspectives into the temporal manifestation of the ORG related to different stages of the phototransduction cascade (15, 16). In addition, imaging anesthetized animals has fewer motion artifacts and is less subjective to lens opaqueness and other ocular complexities.

Despite all the benefits mentioned above, the size of rod outer segments in rodents ($\sim 1.4\,\mu\mathrm{m}$ in diameter) is often smaller than the lateral resolution of the OCT system (17). Hence, the

DRAFT

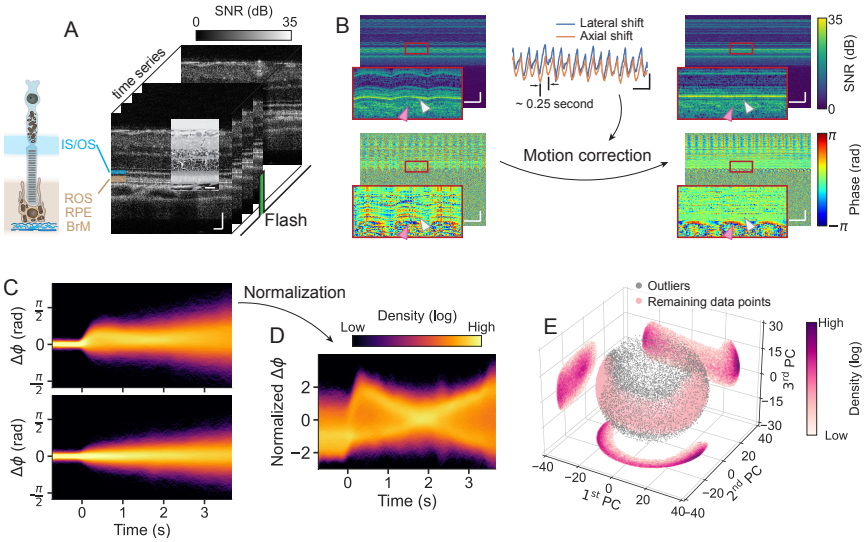


**Fig. 1.** Image and signal processing framework for automated, unbiased optoretinography. (A) Repeated cross-sectional OCT images acquired from a 12° field of view on the rat's retina. In the outer retina, the upper hyperreflective band corresponds to the inner segment/outer segment junction (IS/OS), while the lower hyperreflective band contains the outer segment tips of photoreceptors, retinal pigment epithelium (RPE), and Bruch's membrane (BrM). The OCT structural image agreed well with the histology (inset). Scale bar: $100\,\mu\mathrm{m}$ for OCT images and $20\,\mu\mathrm{m}$ for histology. (B) Left column: time-elapsed intensity (upper) and phase (lower) M-scans without correction, when no light stimulus was delivered to the retina. Scale bar: $500\,\mathrm{ms}$ (horizontal), $100\,\mu\mathrm{m}$ (vertical). Center column: the subpixel-level bulk motion estimated by locating the peak of the upsampled cross-correlation map between repeated B-scans. Scale bar: $500\,\mathrm{ms}$ (horizontal), $5\,\mu\mathrm{m}$ (vertical). Right column: corresponding time-elapsed intensity (upper) and phase (lower) M-scans after the phase-restoring subpixel motion correction. Scale bar: $500\,\mathrm{ms}$ (horizontal), $100\,\mu\mathrm{m}$ (vertical). Gray and pink arrows label loci of the outer retina and the choroid, respectively. (C) The distribution density of stable phase traces with (top) and without (bottom) a light stimulus. (D) The distribution density of normalized phase responses with a light stimulus, after each phase trace in the top panel of Fig. 1C was subtracted by its mean value and divided by its standard deviation. (E) The distribution of the normalized phase responses in the common principal component (PC) space consisting of the top three PCs. Gray dots represent the outliers identified using a distance-based outlier detection method, while remaining data points were labelled by pink dots. The heatmaps show the distribution density of the remaining data points when projected onto three feature planes.

light scattered from multiple rod outer segments is coherently integrated by the point spread function of the OCT system, resulting in obscured speckle patterns in the OCT image. To mitigate the problem, previous reports of the ORG response in rodents mostly relied upon measuring the averaged intensity of photoreceptor layers in the OCT image (1, 18, 19). This method is limited by the axial resolution of the OCT ($\sim 2\,\mu\mathrm{m}$ in air) and cannot provide the nanometer-scale precision achieved in human subjects by measuring phase changes originated from the movements of cone outer segment tips. Although a few studies have extracted phase-sensitive ORG signals from speckle patterns by spatial averaging, this approach could not maintain the spatial heterogeneity (20–22). It was unclear how the actual nanoscopic tissue movement could be interpreted from the phase component of speckle patterns or how other tissues such as the retinal pigment epithelium (RPE) and the Bruch's membrane (BrM) behave in response to light stimuli, as their signals are mixed in these speckle patterns. The randomness of speckle patterns adds further difficulty in identifying the proper pixel for detecting the phase change, which can vary dramatically from one to another. Currently, there is no criterion for picking the right pixel from speckle patterns while minimizing the measurement bias among different animals, which is crucial for preclinical trials.

In this paper, we propose an automated, unbiased approach for studying comprehensive outer retina dynamics in response to visual stimuli in rodents using a phase-sensitive spectral-domain OCT system. We employed a recently developed phase-restoring subpixel motion correction method to correct the bulk tissue motion that would degrade the accuracy of phase measurement in speckle patterns. Moreover, temporal phase traces were extracted from speckle patterns in the outer retina, projected onto a common principal component (PC) space, and automatically classified using hierarchical clustering. To ensure consistency across data from different animals, a support vector machine (SVM) was trained in the same PC space, and the learned decision boundaries were applied to classify all subsequent phase traces. We validated the repeatability of our method and performed comprehensive evaluations under different scotopic and photopic conditions. We also demonstrated *en-face* mapping of the outer retina function in an extended (12°) field of view (FOV), analogous to multifocal electroretinograms.

## Results

**Agglomerative hierarchical clustering and support vector machine in the principal component space enable automated, unbiased optoretinography.** To reveal comprehensive dynamics of the outer retina in response to light stimuli in an unbiased manner, we projected individual phase traces onto a common PC space, and employed unsupervised learning via agglomerative hierarchical clustering to group them into distinct types. A SVM model was then trained on these type labels in the common PC space, enabling us to classify new phase traces with the same decision boundaries (*Methods*, *SI Appendix*, Fig. S1). Cross-sectional (Fig. 1A) or volumetric scans were acquired in time sequence from a 12° FOV on wild-type rats' retinas. We computed

DRAFT

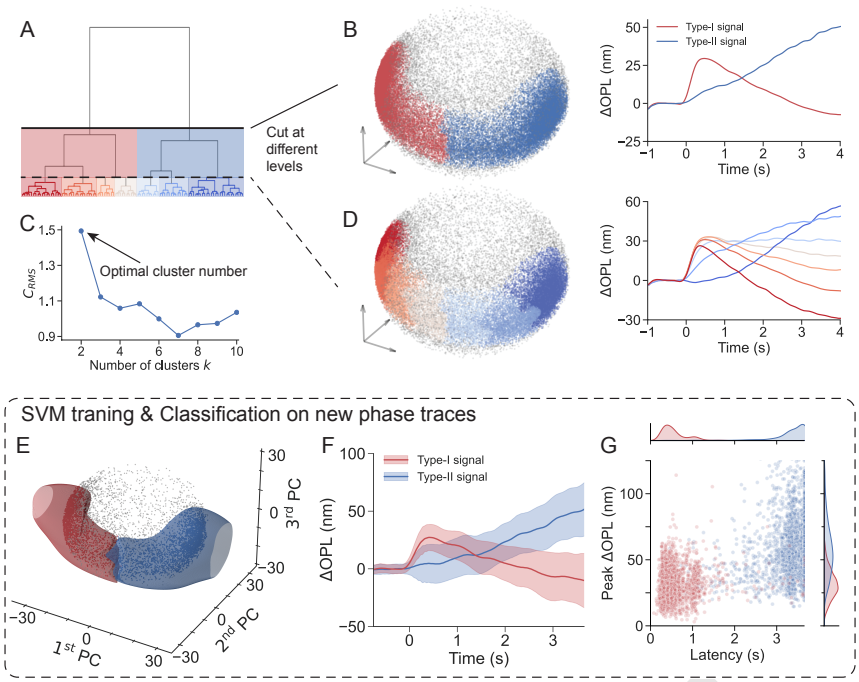


**Fig. 2.** Unsupervised machine learning using agglomerative hierarchical clustering, and subsequent classification on new phase traces using a support vector machine (SVM). (A) Dendrogram showing the cluster structure of phase traces in the common PC space, only the top 100 subclusters are shown. (B) Left: clustering phase traces in the common PC space into 2 clusters by thresholding the dendrogram along the solid black line. Colored dots denote different groups and the gray dots denote outliers. Right: corresponding representative Type-I and Type-II signals obtained by averaging individual phase traces within each cluster. (C) $C_{RMS}$ value with respect to different cluster numbers. The optimal number of clusters was determined by the cluster number offering the maximum $C_{RMS}$ value. (D) Left: clustering phase traces in the common PC space onto 7 clusters by thresholding the dendrogram along the dashed black line. Colored dots denote different groups and the gray dots denote the outliers. Right: corresponding representative signals for each cluster. (E) The trained SVM decision boundaries for Type-I signal (red) and Type-II signal (blue). Dots represent the phase traces extracted from a new dataset and after being preprocessed and projected onto the same PC space. They were classified into Type-I signal (red dots), Type-II signal (blue dots) and outlier (grey dots) using the pre-trained SVM. (F) Representative Type-I (red) and Type-II (blue) signals obtained by averaging individual phase traces within their respective decision boundaries. The solid lines and color bands denote the mean values and the range of standard deviations. (G) The distribution of peak ΔOPLs and corresponding latencies of individual Type-I (red) and Type-II (blue) signals in Fig. 2F.

the phase difference between two hyperreflective bands in the outer retina to reveal its dynamics. As illustrated in Fig. 1A, the upper layer corresponds to the inner segment/outer segment junction (IS/OS) of photoreceptors. The lower layer contains multiple types of tissues that the current imaging modality cannot resolve, including the outer segment tips of the photoreceptors, RPE, and BrM. From here, we call this lower layer the *target layer* for convenience. Despite the high motion detection sensitivity of phase-sensitive OCT, its signal stability is susceptible to bulk tissue motion, which would result in apparent image distortions in the time-elapsed intensity M-scan and degrade the phase stability (see Fig. 1B, left column). To correct the negative influence of bulk tissue motion, we adopted our recently proposed phase-restoring subpixel motion correction method to register complex-valued OCT images down to subpixel precision (23). We noticed periodical oscillations on the order of a few micrometers in estimated lateral and axial shifts that matched the frequency of heart pulsation (∼4 Hz, see Fig. 1B, center column). After image registration (see Fig. 1B, right column), we achieved excellent motion stability at photoreceptor layers (gray arrows), while periodical oscillations from the vascular pulsation (pink arrows) could be observed in the choroid.

For each pixel in the *target layer*, we computed its temporal phase change with respect to the IS/OS layer (*Methods*). To account for inter-subject differences, phase traces from five healthy rats were combined for the subsequent feature extraction and unsupervised clustering. We set a threshold in the pre-stimulus period to remove phase traces with high variance prior to the light stimulus, leaving stable phase traces for further analysis. When a flash was delivered to the retina (t = 0 s), function-associated phase responses were clearly observed (see Fig. 1C, top), whereas without a light stimulus, phase traces were gradually decorrelated without any noticeable response pattern (see Fig. 1C, bottom). Each phase trace in the top panel of Fig. 1C was then normalized by subtracting its mean value and then divided by its standard deviation (SD). The normalization process contrasted two distinct signal patterns in the distribution density map (Fig. 1D). We conducted principal component analysis (PCA) across temporal phase traces and retained the top three components to form a common PC space, as shown in Fig. 1E. To avoid undesirable elongated clusters in subsequent unsupervised clustering, we further used a distance-based outlier detection algorithm to identify and remove outliers distributed in low-density regions (gray dots in Fig. 1E).

To automatically classify remaining phase traces in the common PC space (pink dots in Fig. 1E), we used an agglomerative hierarchical clustering algorithm based on Ward's criterion (24). Thresholding the dendrogram at different levels leads to different clusters (see Figs. 2A-D). For example, Fig. 2D shows the clustering result in the PC space when

DRAFT

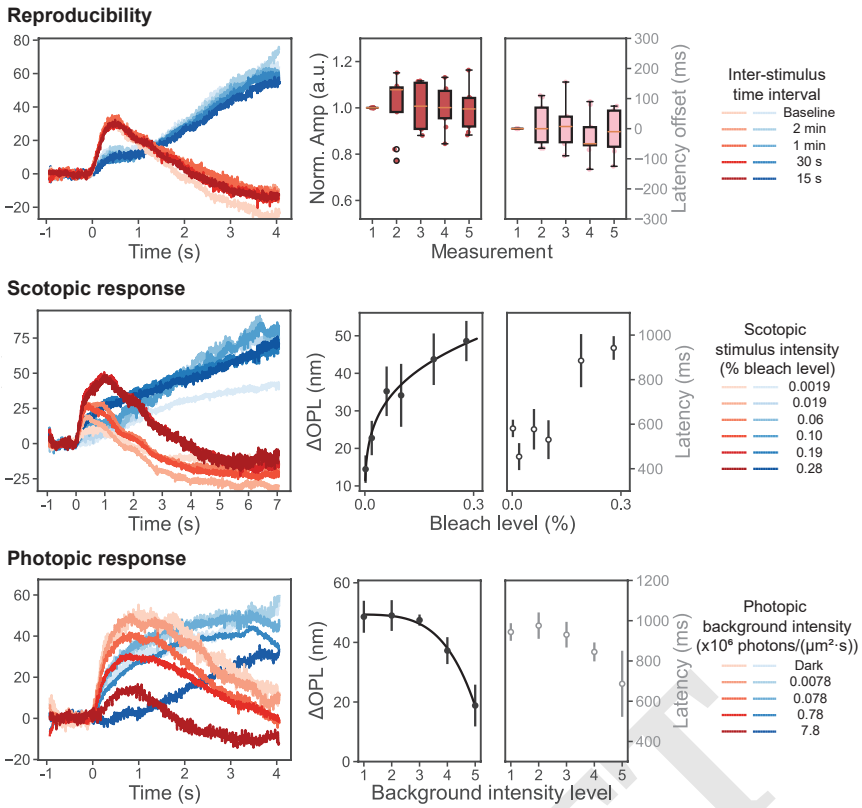


**Fig. 3.** Representative temporal traces of Type-I and Type-II signals, and statistical summaries of peak amplitudes and latencies of Type-I signals. (A) Results of repeated measurements from the same location but varying inter-stimulus time intervals. Both Type-I and Type-II signals were consistent over measurements. The statistical summary from six animals showed no change in either peak amplitude or latency. (B) Results with different flash intensities after dark adaptation (scotopic condition). Peak amplitude increased nonlinearly with increasing bleach levels, and a solid curve is the best fit to $y = ax^c/(x+b)$. The amplitude approached saturation when the bleach level was at 0.28%. Peak latency was relatively stable at a breach level $\leq$ 0.10% and started to increase at a breach level $\geq$ 0.19%. (C) Results with the same flash intensity (breach level = 0.28%) after 5 minutes of light adaptation under different background intensities (photopic conditions). A background intensity of $7.8 \times 10^3$ $\mathrm{photons/(\mu m^2 \cdot s)}$ didn't cause a significant change in the response. The Type-I signal got attenuated and recovered faster with higher background intensities. For box plots, pink bar: mean value, box edges: 25 and 75 percentiles, whisker: 1.5 × standard deviations (SDs). For scatter plots, error bar: 1 SD.

DRAFT

phase traces were divided into 7 groups along the dashed black line in Fig. 2A. Corresponding representative signals were obtained by averaging individual phase traces within each cluster and converted into the optical path length change (ΔOPL), where two distinct types (red and blue) and some intermediate types were detected. To find out the optimal cluster number for further quantitative analysis, we calculated inter-cluster correlation coefficients between representative signals and computed their root-mean-square (RMS) relative to 1 (perfect correlation), which is termed $C_{RMS}$. A higher $C_{RMS}$ indicates a larger inter-cluster dissimilarity. As shown in Fig. 2C, when the cluster number was 2, $C_{RMS}$ reached its maximum to best distinguish representative signals. Therefore, we applied a threshold to the dendrogram (solid black line in Fig. 2A) to divide the phase traces in the PC space into 2 clusters (Fig. 2B). The first type of signal (red) exhibited a biphasic trend with a rapid elongation followed by a gradual recovery, while the second type of signal (blue) showed a slow elongation. In this study, we named these two types of signals *Type-I* and *Type-II* signals.

We later trained a support vector machine (SVM) model with the labels obtained in Fig. 2B to set boundaries for Type-I signal (red surface) and Type-II signal (blue surface) in the common PC space, as shown in Fig. 2E. Using the pre-trained SVM, preprocessed new phase traces can be successfully classified into Type-I signal (red dots within the red decision boundary in Fig. 2E), Type-II signal (blue dots within the blue decision boundary in Fig. 2E), and outlier (grey dots in Fig. 2E) in the identical PC space. Figure 2F shows average phase traces of the classified Type-I signals (red) and Type-II signals (blue), with their bands showing their standard deviations (SDs). The peak amplitudes and corresponding latencies of individual Type-I and Type-II signals exhibited a clear separation (Fig. 2G).

**Signal repeatability and dependencies on experimental conditions in scotopic and photopic environments.** We tested the reproducibility of Type-I and Type-II signals by repeating the measurement 5 times at the same location. We maintained equal stimulus intensity (0.10%, 1 ms) across all 5 trials, and we shortened time intervals between flashes progressively from 2 minutes to 15 seconds. As shown in Fig. 3A, both Type-I and Type-II signals were reproducible across acquisitions ($p > 0.05$, *repeated measures analysis of variance*), and the variance across the traces increased slightly over time, which was likely due to progressive signal decorrelation from motion. For statistical analysis, we compared with baseline to calculate the fractional change in the peak amplitude and the offset in the peak latency, avoiding inter-animal variation. The peak amplitude and latency

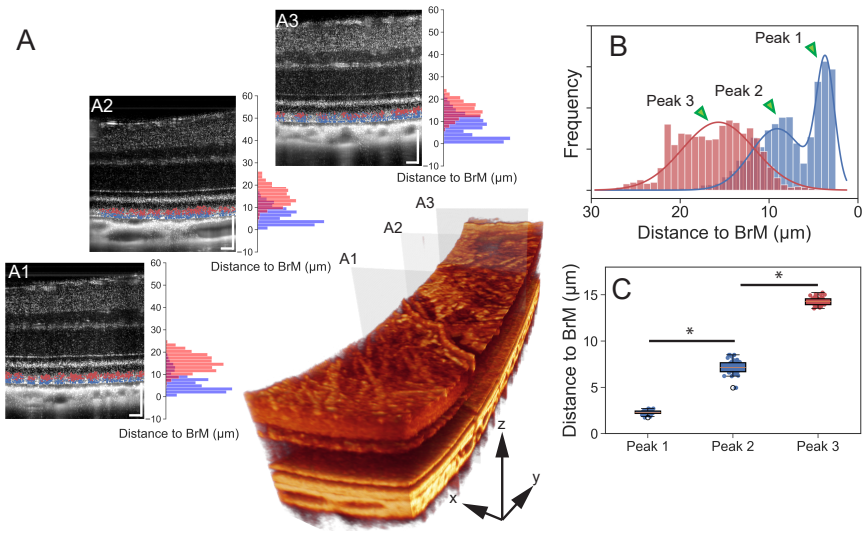


**Fig. 4.** The depth distribution of Type-I and Type-II signals in retina cross-sections. (A) Representative OCT images at cross-sections A1, A2, and A3 with loci of Type-I (red dots) and Type-II (blue dots) signals labeled. Type-I signals were located more anteriorly than Type-II signals. Histograms of their axial distances to BrM are shown in the vertical axis. Scale bar: $50\,\mu\mathrm{m}$. (B) The histogram of Type-I loci showed a normal distribution, and the histogram of Type-II loci showed two distinct peaks, which can be fitted in a bimodal Gaussian distribution. (C) The loci of the three peaks differed significantly from each other (*P < 0.05).

of the Type-I signal stayed consistent among measurements. Normalized peak amplitude fluctuation was at a maximum of 0.107, and the peak latency fluctuation was at a maximum of 78 ms.

Next, we tested the dependencies of Type-I and Type-II signals on light stimulus strengths in the scotopic condition. Type-I and Type-II signal traces in response to different levels of stimulus strengths are shown in Fig. 3B. For the Type-I signal, the peak amplitude increased non-linearly with higher stimulus strengths, where $\Delta$OPL was 14.46 (3.66) nm [mean (SD)] at a bleach level of 0.0019%, and approached the saturation level of 48.60 (5.36) nm when the bleach level increased 148-fold to 0.28%. The peak latencies remained within 450 – 580 ms at a bleach level $\leq$ 0.10%, but in response to stronger stimuli at 0.19% and 0.28% bleach, the latency increased to 885.3 (119.3) ms and 892.1 (53.1) ms, respectively. Interestingly, a negative-going wave that followed the positive peak was sensitive to the stimulus intensity, and a stronger stimulus was associated with a less negative $\Delta$OPL. In contrast, the monophasic Type-II signal appeared to have a slow and gradient slope at a bleach level of 0.0019%, and the slope seemed to stabilize at bleach levels between 0.019% to 0.10%. At a higher bleach level $\geq$ 0.19%, the Type-II signal underwent an initial rapidly rising slope, followed by a slow ramp.

Moreover, we tested the dependencies of Type-I and Type-II signals on background intensities in photopic conditions. A series of Type-I and Type-II signal traces with different levels of light adaptation are shown in Fig. 3C. The light adaptation lasted for 5 minutes using the same LED (500 nm) before each flash stimulus. The background intensities ranged from $7.8\times10^3$ to $7.8\times10^6\,\mathrm{photons/(\mu m^2{\cdot}s)}$, while the stimulus strength was identical across these tests (bleach level = 0.28%). With the dimmest background illuminance ($7.8\times10^3\,\mathrm{photons/(\mu m^2{\cdot}s)}$), no significant change was detected. With brighter light adaptation intensities, the Type-I signal started to attenuate: the peak amplitude decreased from 48.60 (5.36) nm to 18.8 (7.0) nm, and the recovery was faster with the peak latency decreased from 892.1 (53.1) ms to 686.5 (164.1) ms. The Type-II signal, in contrast, stayed relatively consistent when background intensities $\leq 7.8\times10^5\,\mathrm{photons/(\mu m^2{\cdot}s)}$, and an apparent smaller slope appeared with a brighter background illuminance of $7.8\times10^6\,\mathrm{photons/(\mu m^2{\cdot}s)}$.

**Spatial and depth-resolved retinal function maps over an extended field of view.** We explored spatial distributions of Type-I and Type-II signals in retina cross-sections (Fig. 4). Figure 4A shows an OCT volume of a rat's retina, where ORG experiments were conducted in sequence on adjacent cross-sectional scans. The bleach level was 0.10%, and the time interval between acquisitions was 2 minutes. Red and blue dots in OCT cross sections in Fig. 4A show the loci of Type-I and Type-II signals and histograms (insets) show their axial distances to BrM. We found that Type-I signals were located more anteriorly than Type-II signals. More specifically, Type-I loci obeyed a normal distribution, while Type-II loci showed two distinct peaks, which could be fitted in a bimodal Gaussian function (blue curve in Fig. 4B). The loci of the three peaks differed significantly from each other (Fig. 4C, *P < 0.05, *analysis of variance and Bonferroni post-hoc comparison*). As a comparison, we calculated averaged traces stratified by their distances to BrM (*SI Appendix*, Fig. S2), traces similar to Type-I and Type-II signals were observed at depths distal and proximal to BrM, respectively. From a distance of 4.47 - 17.87 μm to BrM, traces appeared as a mixture of Type-I and Type-II signals.

In an *en-face* fashion, we achieved automated ORG in volumetric OCT scans offering geographic function maps, analogous to multifocal electroretinograms but only required a single-shot measurement (Fig. 5). Figure 5A shows an OCT volume with 12° FOV, with the structural contrast in

DRAFT

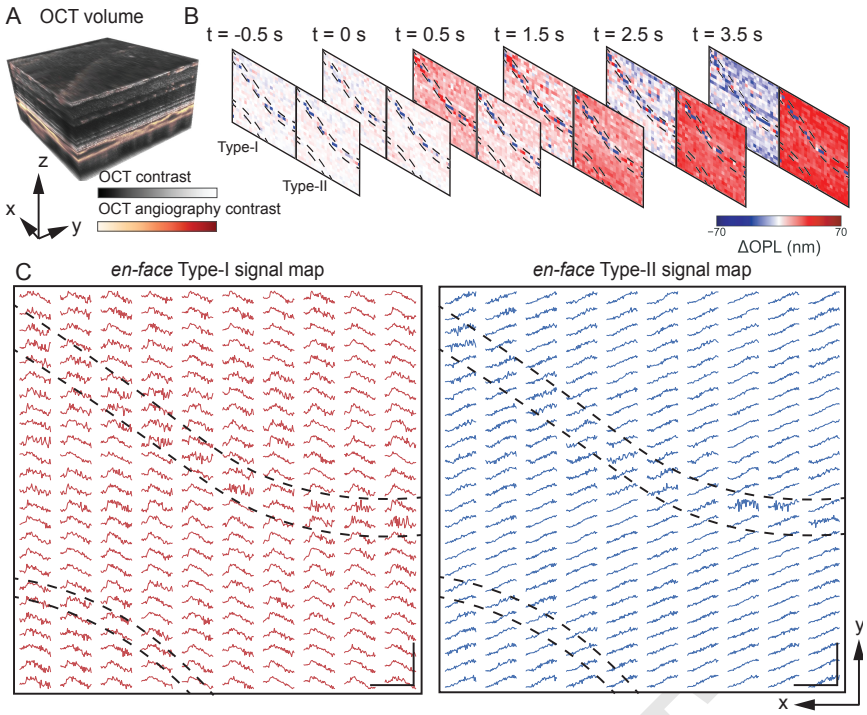


**Fig. 5.** Representative *en-face* maps of Type-I and Type-II signals. (A) A volumetric scan covered a 12° field of view (FOV), where locations blocked by large superficial vessels were labeled in dashed lines (Figs. 5B and 5C). (B) The spatial distribution of Type-I and Type-II signals at selected time points, and its complete temporal evolution is shown in the *Movie S1*. Each grid represents the averaged response from 1.2° × 0.48° FOV. (C) Spatiotemporal evolution of Type-I and Type-II signals extracted over the entire FOV. Signals underneath large vessels (outlined by dashed lines) exhibited higher variations because of signal decorrelation. Each curve corresponds to the averaged response from 1.2° × 0.48° FOV. Scale bar: $200\,\mu\mathrm{m}$.

gray scale and angiographic contrast highlighted in red color. Phase traces were extracted from repeated volumetric scans and classified into Type-I signal, Type-II signal and outlier (*Methods* and *SI Appendix*, Fig. S3). Figures 5B and 5C depict the corresponding temporal evolution of the extracted Type-I and Type-II signals, where the classified temporal phase traces were averaged into 10 × 25 ($x \times y$) grids, each of which represents the outer retina response from a 1.2° × 0.48° area. In general, our *en-face* automated ORG showed high-fidelity detection over the entire FOV, except for regions underneath large vessels (dashed lines; Figs. 5B and 5C) because of signal decorrelation. A video visualizing the spatiotemporal evolution of Type-I and Type-II signals is shown in *Movie S1*. Phase signals during the pre-stimulus period were highly stable over the entire FOV except for regions outlined by dashed lines. After the stimulus, Type-I signals peaked within 1 second and returned below the baseline at t = 3.5 seconds. In contrast, Type-II signals showed a slow, monotonical increase until t = 3.5 seconds.

## Discussion

In this paper, we demonstrated an automated, unbiased ORG for rodents using a point-scan, phase-sensitive, spectral-domain OCT. Using our approach, two types of signals that corresponded to the dynamics of different tissue types in rodents were automatically identified from speckle patterns, in which the fast Type-I signal has not been previously reported. A SVM model was trained to explore the decision boundaries of each type of signal in an established PC space, facilitating the automated classification of phase traces in new datasets. We simultaneously studied outer retinal dynamics containing various tissue types. Moreover, we generated geographic function maps, analogous to multifocal electroretinograms, with only a single-shot measurement as brief as a few seconds. We demonstrated a general protocol applicable to conventional OCT systems in animal labs and clinics without any demanding hardware. Our method holds a remarkable potential in mining for tissue-specific dynamics to other stimuli/triggers of interest from noisy speckle patterns.

Rod phototransduction cascade was studied pharmacologically, electroretinographically, and genetically (25, 26). Investigating rod ORG is difficult in human subjects because rods are generally denser, smaller, and packed around cones (27, 28). One recent study demonstrated rod dynamics using ORG combined with hardware-based adaptive optics (17). The authors reported that rods exhibited a faster response and lower saturation threshold than cones in human subjects. Since rod's structure and function are almost identical among vertebrate animals, nocturnal animals like rodents, which possess a high percentage of rods (∼97%) (11), are optimal for studying rod dynamics. The remaining 3% cone population, especially the M-opsin, which shares the same spectral sensitivity with rods, could potentially contribute to the detected signal. However, our data showed that the Type-I signal approaches saturation with meager bleach levels (0.28%) and is significantly influenced by dim background illuminance ($\geq 7.8 \times 10^5\ \mathrm{photons}/(\mu\mathrm{m}^2{\cdot}\mathrm{s})$). These pieces of evidence indicate a minimal contribution from cones, since cones have a higher saturation level and their responses are

DRAFT

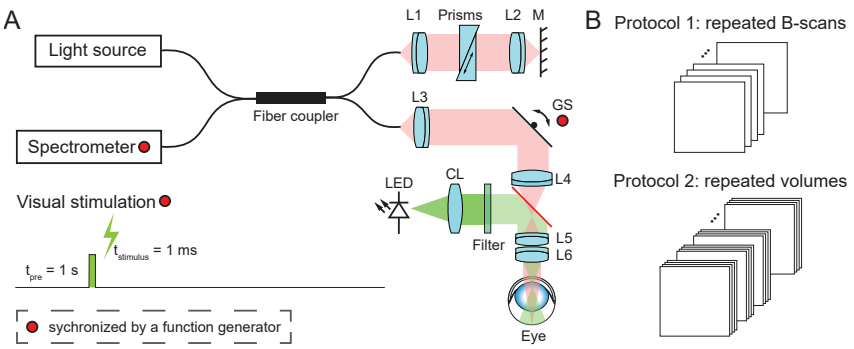


**Fig. 6.** System setup, stimulus scheme and acquisition protocols. (A) An ultrahigh-axial-resolution spectral-domain OCT was used to image the posterior eye. A line-scan camera interfaced with the spectrometer was used to acquire the interference fringe. A function generator synchronized the line-scan camera acquisition, galvo scanner rotation, and flash timing. L1-L6: doublet lenses. CL: condenser lens. GS: galvo scanner. Filter spectral window: 500 ± 5 nm. (B) Two acquisition protocols were used: repeated B-scans (Protocol 1: 1000 A-scans per B-scan, 200 B-scans per second) and repeated volumes (Protocol 2: 1000 A-scans per B-scan, 25 B-scans per volume, 8 volumes per second). The details of acquisition and stimulation protocols were listed in *SI Appendix*, Table S3.

less attenuated by background illuminance (29). Moreover, M-opsin expression decreases progressively from dorsal to ventral retina, whereas the rhodopsin distribution is uniform over the entire retina (30). The evenly distributed Type-I signals detected from our OCT volumes (12° FOV) further corroborates the dominance of rods' contribution to the Type-I signal.

Some recent studies reported photoreceptor dynamics in rodents using intensity or phase information (1, 20, 31). By massively averaging the intensity profiles among A-scans (1) or phases within the region of interest (20), a slow and gradient elongation of the outer segment was observed (1). Ma et al. applied prior knowledge of early signal activation to select temporal traces and found a fast onset (2 ms) followed by a consistent increase/decrease of the intrinsic tissue scattering (31). The benefits of using phase information and performing unsupervised clustering in the PC space based on non-averaged temporal traces arise from the following aspects: (i) phase change is more sensitive to the nanoscopic tissue movement in the axial direction, and has an intuitive and quantitative relationship with the moving distance. (ii) as mentioned above, rod outer segment dynamics are compounded by motion from other tissues in a conventional OCT image due to insufficient resolution, and an automated classification algorithm could isolate the rod signal from other confounders without requiring prior knowledge.

Elongation of outer segment tips is associated with the activation of phototransduction that can be modeled by a collective effect of osmotic pressure imbalance and restoring force between macromolecules (1). A more recent study hypothesized that the photoreceptor elongation is an aggregated effect of osmotic water influx, membrane swelling, transmembrane water transport via activated rhodopsin, and water influx via choroidal vasculature (3). Our experiment measured a saturated elongation of $\sim 34$ nm (calculated with a refractive index of 1.41) at 1 second. Based on a previous model developed by Zhang et al. and assuming similar parameters, including the rest plasma osmolarity (325 mOsM) (32) rod length ($24.0\,\mu\mathrm{m}$), rod OS cross-sectional area ($1.54\,\mu\mathrm{m}^2$) (1) and rod OS surface area ($132\,\mu\mathrm{m}^2$), we achieved a water permeability coefficient of $5.8 \times 10^{-3}\,\mathrm{cm{\cdot}s^{-1}}$, which is about 250-fold higher than in (1) but similar to $2.6 \times 10^{-3}\,\mathrm{cm{\cdot}s^{-1}}$ observed from in-vitro studies (33, 34). Details are shown in *SI Appendix* and *SI Appendix*, Table S1. We also observed a faster and full recovery of the rod elongation: the signal recovered to the baseline or even lower within 4 seconds. A plausible explanation is the rebinding of the osmolytes during deactivation (25, 26). However, the understanding for the Type-II signal is still lacking as the response is likely derived from non-photosensitive tissues, including RPE, and BrM. The slow and progressive shift of their positions may originate from transport of water through pigment epithelial cells into the subretinal space around photoreceptors (35–37).

## Methods

**System setup.** A custom-built spectral-domain optical coherence tomography performed all imaging experiments in this study (Fig. 6). The system operated with a broadband superluminance diode (cBLMD-T-850-HP-I, $\lambda_c$ = 850 nm, $\Delta\lambda$ = 165 nm, Superlum, Ireland), providing an axial resolution of $1.4\,\mu\mathrm{m}$ in tissue. A spectrometer interfaced with a line-scan camera (2048 pixels, 250,000Hz, Octoplus, E2V) acquired the spectral interference fringes, corresponding to an image depth of 1.07 mm in air. For posterior eye imaging in rodents, a pair of telescopic lenses conjugated the axis of galvo scanner to the pupil. The magnification of the telescopic lenses was 0.17 (scan lens: 80 mm focal length; ocular lens: 30 mm + 25 mm focal length) to shrink the incident beam size and increase the scan angle. The theoretical diffraction-limited lateral resolution was $7.2\,\mu\mathrm{m}$ with a standard rat eye model (38). A function generator (PCIe-6363, National Instrument, USA) synchronized the camera acquisition (both A-scan and B-scan acquisitions), galvometer scanning, and visual stimulation.

For visual stimulation, a LED (MBB1L3, Thorlabs, USA) was collimated by an aspheric condenser lens, and a narrow bandpass filter (500 ± 5 nm, #65-694, Edmund Optics, Singapore) was used to reshape the spectrum to optimize the sensitivity to rhodopsin (39). The LED's response time was $\sim$300 µs, equivalent to 6% of the B-scan frame acquisition time, and LED's response waveform to trigger is shown in

DRAFT

*SI Appendix*, Fig. S4. A 43.4° Maxwellian illumination was projected to the posterior eye to cover an area of approximately $6.75\,\mathrm{mm}^2$. The power and duration of the light stimulus were converted to bleach percentages using published method (40, 41), which is detailed in *SI Appendix*.

**Animal experiment protocol.** All experiments were conducted in accordance with guidelines and approvals from Institutional Animal Care and Use Committee (IACUC), SingHealth (2020/SHS/1574). Brown Norway rats (N = 37) were used with details listed in *SI Appendix*, Table S2). The animals were sedated using a ketamine/xylazine cocktail. The selection of ketamine/xylazine for anesthesia is to better maintain retinal functional responses compared to other commonly used anesthetics, such as isoflurane and urethane, while minimizing eye motion (42, 43). Vital signals, including heart rate and respiration rate, were monitored throughout the imaging sessions. The animals were placed in a prone position with their head restrained stereotaxically. The scanning region was limited to the dorsal area to avoid interference from S-opsin and M-opsin spectrally and spatially (39). Two mydriasis drops, each of 1% Tropicamide (Alcon, Geneva, Switzerland) and 2.5% Phenylephrine (Alcon, Geneva, Switzerland), were administrated onto the cornea before the imaging. The cornea was moisturized using a balanced salt solution frequently throughout the imaging sessions.

Details of the acquisition and stimulation protocols are listed in *SI Appendix*, Table S3. Two scanning protocols, repeated B-scans and repeated volumetric scans, were used in this study. Both protocols have the same frame rate (1000 A-scans per B-scan, 200 B-scans per second). The former protocol performed repeated scans at one cross-section and the later protocol consisted of 40 repeated volumes (25 B-scans per volume), corresponding to 8 volumetric scans per second for a period of 5 seconds. Flash intensity, dark/light adaptation and inter-stimulus time interval varied in different experiments.

### Automated extraction of comprehensive outer retina dynamics from speckle patterns.

***Preprocessing of OCT images and phase traces.*** The raw interference fringe first underwent standard OCT post-processing steps, including spectral calibration, k-linearity, dispersion compensation, and discrete Fourier transform (DFT), which resulted in complex-valued OCT images.

To correct the motion-induced phase error in speckle patterns caused by bulk tissue motion, we estimated subpixel-level translational displacements between repeated B-scans using the single-step DFT algorithm (44). We registered the complex-valued OCT images using our recently developed phase-restoring subpixel motion correction approach (23), where the lateral and axial displacements were corrected by multiplying the corresponding exponential terms in the spatial frequency domain and the spectrum domain, respectively. Light-evoked dynamics of the outer retina was then extracted out by computing the temporal phase difference between the pixel pairs from two highly reflective outer retinal bands. One from IS/OS, and the other, termed *target layer*, from a complex layer containing photoreceptor outer segment, RPE and BrM (see Fig. 1A). These two layers can be automatically segmented based on graph theory and dynamic programming (*SI Appendix*, Fig. S1A) (45).

For each pixel of interest in the *target layer*, we selected a region from IS/OS that centered at the same A-line as a reference region. Each reference region comprised of 5 adjacent A-lines ($\sim$7.1 µm laterally). Before conducting spatial averaging across the reference region, we cancelled out the systematic phase drift by self-referencing and removed arbitrary phase offset of individual phase trace by referring to its pre-stimulus frames. Specifically, the systematic phase drift was canceled out by calculating the multiplication of the complex-valued OCT signal of the pixel of interest in the *target layer* and the complex conjugate of the signals in the selected reference region,

$$\tilde{I}_{tar/\mathrm{ISOS}}(s,i) = \tilde{I}_{tar}(i)\tilde{I}^{*}_{\mathrm{ISOS}}(s,i), \quad \textbf{(1)}$$

where $\tilde{I}_{tar}(i)$ is the complex-valued OCT signal of the pixel of interest in the *target layer*, $i$ is the index of the frame number. $\tilde{I}_{\mathrm{ISOS}}(s,i)$ represents signals in the corresponding reference region, and $s$ denotes the pixel index in the reference region. $\tilde{I}_{tar/\mathrm{ISOS}}(s,i)$ is the pairwise self-referenced signal, where the pixel of interest in the *target layer* was ergodically referred to all pixels in its reference region. * represents complex conjugate.

To cancel out arbitrary phase offsets, each complex-valued signal trace was referred to its pre-stimulus frames,

$$\Delta\tilde{I}_{tar/\mathrm{ISOS}}(s,i) = \tilde{I}_{tar/\mathrm{ISOS}}(s,i)\cdot\frac{1}{N}\sum_{i=1}^{N}\tilde{I}^{*}_{tar/\mathrm{ISOS}}(s,i), \quad \textbf{(2)}$$

where $\Delta\tilde{I}_{tar/\mathrm{ISOS}}(s,i)$ denotes time referenced signals, $N$ represents the number of frames acquired before the light stimulus. The complex-valued signals were subsequently averaged across pixels in the reference region, and the phase information was extracted from the averaged complex-valued signal,

$$\Delta\tilde{I}_{tar/\mathrm{ISOS}}(i) = \frac{1}{S}\sum_{s=1}^{S}\Delta\tilde{I}_{tar/\mathrm{ISOS}}(s,i), \quad \textbf{(3)}$$

$$\Delta\phi(i) = \angle\Delta\tilde{I}_{tar/\mathrm{ISOS}}(i), \quad \textbf{(4)}$$

where $\Delta\phi(i)$ is one phase trace extracted from the pixel of interest in the *target layer*. $S$ is the total pixel number in the reference region, $\angle$ represents the calculation of argument.

We applied the same process to each pixel in the *target layer* to extract spatial-resolved temporal phase traces. Once the individual phase traces were obtained, they can be converted into the OPL change $\Delta\mathrm{OPL}(i)$ by,

$$\Delta\mathrm{OPL}(i) = \frac{\lambda_0}{4\pi}\Delta\phi(i), \quad \textbf{(5)}$$

DRAFT

where $\lambda_0$ is the central wavelength of the OCT system.

We also conducted temporal filtering to remove unwanted signal frequencies. The extracted signals were first processed by bandstop filters to minimize residual artifacts induced by heartbeat and breathing. A low-pass filter with a cut-off frequency of 10 Hz was subsequently used to filter out high-frequency oscillations. After filtering, both ends of the phase traces exhibited high variance due to edge effects, so they were removed from the data analysis afterwards (*SI Appendix*, Fig. S1C). Traces with a pre-stimulus SD larger than 60 mrad were excluded. Each phase trace was normalized by subtracting its mean value and then dividing by its SD, thereby removing the difference in amplitude.

***Feature extraction using the principal component analysis.*** We used the PCA to compress high-dimensional phase traces into a lower-dimensional feature space to facilitate the analysis. To account for inter-subject differences, we combined normalized phase traces extracted from five healthy rats to calculate PC coefficients. The top three PCs capturing a total variance of 83.1% were selected to constitute a common PC space. This variance is only 0.3% smaller than projecting each dataset onto its own unique PC space, indicating great consistency among datasets.

To avoid undesirable elongated clusters in subsequent unsupervised clustering analysis, we used a distance-based outlier detection method to preclude outliers distributed in low-density regions in the common PC space (46, 47). For each data point in the common PC space, we calculated the minimum radius of a sphere that centered at that point and can cover 2% of the remaining data points. This radius reflected the local distribution density around each data point in the common PC space. Then, a given point would be labeled as an outlier if its corresponding radius was larger than $Q_3 + (Q_3 - Q_1)/5$, where $Q_1$ and $Q_3$ are the first and third quartiles of the calculated radii.

***Unsupervised clustering with a hierarchical clustering algorithm.*** We used an agglomerative hierarchical clustering algorithm under the Ward criterion to group individual points in the common PC space (24). The Euclidean distance of each pair of points was computed and similar subclusters were then iteratively merged into larger clusters. Under the guidance of the Ward method or minimum variance method, each merger guaranteed a minimum increase of total within-cluster variance.

After generating the agglomerative hierarchical cluster tree, we cut off the dendrogram at different levels to yield different clustering results. For each clustering result, corresponding representative phase signals can be obtained by averaging individual filtered phase traces within each cluster. Many methods and criteria have been proposed to determine the optimal cluster number (48). Here, we sought to find the optimal cluster number that maximized the overall inter-cluster dissimilarity between the representative phase signals. Specifically, the pairwise Pearson's cross-correlation coefficient $\rho$ was calculated for all $n_c = (k-1)k/2$ combinations of the representative phase signals, where $k$ is the cluster number. The root-mean-square (RMS) error of those cross-correlation coefficients relative to 1 (perfect correlation) was calculated by (49),

$$C_{RMS} = \sqrt{\frac{\sum_{n=1}^{n_c}(\rho_n - 1)^2}{n_c}}, \tag{6}$$

The cluster number with the largest $C_{RMS}$ was determined as the optimal cluster number.

***Training a support vector model in the established principal component space.*** We trained a SVM in the common PC space with the previously obtained labels, including outlier, Type-I signal, and Type-II signal, to obtain their decision boundaries. The input features were standardized before training, the Gaussian kernel was selected, and automatic hyperparameters optimization was turned on. Evaluated with the 10-fold cross-validation strategy, the trained SVM achieved a classification accuracy of 99.5%. The SVM is useful when we want to process a new dataset using the same criterion. Phase traces extracted from the new dataset will be preprocessed and projected onto the same common PC space. Then Type-I and Type-II signals can be automatically extracted based on the classification results from the SVM.

***Processing of volumetric scans dataset.*** Volumetric scans (protocol 2) had a 25-fold lower temporal sampling rate than repeated B-scans (protocol 1), so we modified the pipeline to classify phase traces from volumetric scans (*SI Appendix*, Fig. S3). The top three PCs from protocol 1 (*SI Appendix*, Fig. S1D) were downsampled by a factor of 25 to form a new PC space. Phase traces from five healthy rats in protocol 1 were also downsampled by a factor of 25 and projected onto the new PC space as features for SVM. Labels were inherited from the classification results obtained in 3.1-3.4. Other procedures were the same as 3.4, and a classification accuracy of 83.4% was achieved.

**ACKNOWLEDGEMENTS**

We thank Drs. R. Sabesan, D. Palanker, A. Roorda, and M. Ismail for fruitful discussions. T. Ling acknowledges the support of the National Research Foundation, Singapore for the NRF Fellowship Award (NRF-NRFF14-2022-0005), the Startup Grant (SUG) from Nanyang Technological University, and the seed funding programme under NMRC Centre Grant – Singapore Imaging Eye Network (SIENA) (NMRC/CG/C010A/2017).

L. Schmetterer acknowledges the funding support for the National Medical Research Council (CG/C010A/2017_SERI; OFIRG/0048/2017; OFLCG/004c/2018; TA/MOH-000249-00/2018 and MOH-OFIRG20nov-0014), National Research Foundation Singapore (NRF2019-THE002-0006 and NRF-CRP24-2020-0001), A*STAR (A20H4b0141), the Singapore Eye Research Institute & Nanyang Technological University (SERI-NTU Advanced Ocular Engineering (STANCE) Program), the Duke-NUS Medical School (Duke-NUS-KP(Coll)/2018/0009A), and the SERI-Lee Foundation (LF1019-1) Singapore.

V. A. Barathi acknowledges the support for Singapore NMRC Centre Grant (NMRC/CG/M010/2017/Pre-Clinical).

**AUTHOR CONTRIBUTIONS**

B.T., H.L., L.S. and T.L. designed the study. B.T. and L.S. built the setup. B.T., H.L. conducted the experiments. V.A.B supported the animal preparation and histology. B.T., H.L and T.L. analyzed the data. B.T., H.L., L.S. and T.L. wrote the manuscript. All work was supervised by T.L. and L.S.

**COMPETING FINANCIAL INTERESTS**

All authors declare no competing financial interests.

DRAFT

# References


1. Pengfei Zhang, Robert J. Zawadzki, Mayank Goswami, Phuong T. Nguyen, Vladimir Yarov-Yarovoy, Marie E. Burns, and Edward N. Pugh. In vivo optophysiology reveals that g-protein activation triggers osmotic swelling and increased light scattering of rod photoreceptors. *Proceedings of the National Academy of Sciences*, 114(14):E2937–E2946, 2017. doi: 10.1073/pnas.1620572114.
2. Vimal Prabhu Pandiyan, Aiden Maloney-Bertelli, James A. Kuchenbecker, Kevin C. Boyle, Tong Ling, Zhijie Charles Chen, B. Hyle Park, Austin Roorda, Daniel Palanker, and Ramkumar Sabesan. The optoretinogram reveals the primary steps of phototransduction in the living human eye. *Science Advances*, 6(37):eabc1124, 2020. doi: 10.1126/sciadv.abc1124.
3. V. P. Pandiyan, P. T. Nguyen, Jr. Pugh, E. N., and R. Sabesan. Human cone elongation responses can be explained by photoactivated cone opsin and membrane swelling and osmotic response to phosphate produced by rgs9-catalyzed gtpase. *Proc Natl Acad Sci U S A*, 119(39):e2202485119, 2022. ISSN 1091-6490 (Electronic) 0027-8424 (Linking). doi: 10.1073/pnas.2202485119.
4. Furu Zhang, Kazuhiro Kurokawa, Ayoub Lassoued, James A. Crowell, and Donald T. Miller. Cone photoreceptor classification in the living human eye from photostimulation-induced phase dynamics. *Proceedings of the National Academy of Sciences*, 116(16):7951–7956, 2019. doi: 10.1073/pnas.1816360116.
5. A. Lassoued, F. Zhang, K. Kurokawa, Y. Liu, M. T. Bernucci, J. A. Crowell, and D. T. Miller. Cone photoreceptor dysfunction in retinitis pigmentosa revealed by optoretinography. *Proc Natl Acad Sci U S A*, 118(47), 2021. ISSN 1091-6490 (Electronic) 0027-8424 (Linking). doi: 10.1073/pnas.2107444118.
6. Mehdi Azimipour, Justin V. Migacz, Robert J. Zawadzki, John S. Werner, and Ravi S. Jonnal. Functional retinal imaging using adaptive optics swept-source oct at 1.6 mhz. *Optica*, 6(3): 300–303, 2019. doi: 10.1364/OPTICA.6.000300.
7. Dierck Hillmann, Hendrik Spahr, Clara Pfäffle, Helge Sudkamp, Gesa Franke, and Gereon Hüttmann. In vivo optical imaging of physiological responses to photostimulation in human photoreceptors. *Proceedings of the National Academy of Sciences*, 113(46):13138–13143, 2016. doi: 10.1073/pnas.1606428113.
8. Donald T. Miller and Kazuhiro Kurokawa. Cellular-scale imaging of transparent retinal structures and processes using adaptive optics optical coherence tomography. *Annual Review of Vision Science*, 6(1):115–148, 2020. doi: 10.1146/annurev-vision-030320-041255.
9. Jessica IW Morgan, Toco YP Chui, and Kate Grieve. Twenty-five years of clinical applications using adaptive optics ophthalmoscopy. *Biomedical Optics Express*, 14(1):387–428, 2023. ISSN 2156-7085.
10. Yuan-Zhi Liu, Fredrick A. South, Yang Xu, P. Scott Carney, and Stephen A. Boppart. Computational optical coherence tomography [invited]. *Biomedical Optics Express*, 8(3):1549–1574, 2017. doi: 10.1364/BOE.8.001549.
11. Yingbin Fu and King-Wai Yau. Phototransduction in mouse rods and cones. *Pflügers Archiv - European Journal of Physiology*, 454(5):805–819, 2007. ISSN 1432-2013. doi: 10.1007/s00424-006-0194-y.
12. Christine A Curcio, Nancy E Medeiros, and C Leigh Millican. Photoreceptor loss in age-related macular degeneration. *Investigative ophthalmology & visual science*, 37(7):1236–1249, 1996. ISSN 1552-5783.
13. P. Tanna, R. W. Strauss, K. Fujinami, and M. Michaelides. Stargardt disease: clinical features, molecular genetics, animal models and therapeutic options. *Br J Ophthalmol*, 101 (1):25–30, 2017. ISSN 1468-2079 (Electronic) 0007-1161 (Print) 0007-1161 (Linking). doi: 10.1136/bjophthalmol-2016-308823.
14. J. Sancho-Pelluz, B. Arango-Gonzalez, S. Kustermann, F. J. Romero, T. van Veen, E. Zrenner, P. Ekstrom, and F. Paquet-Durand. Photoreceptor cell death mechanisms in inherited retinal degeneration. *Mol Neurobiol*, 38(3):253–69, 2008. ISSN 0893-7648 (Print) 0893-7648 (Linking). doi: 10.1007/s12035-008-8045-9.
15. B. Chang, M. S. Dacey, N. L. Hawes, P. F. Hitchcock, A. H. Milam, P. Atmaca-Sonmez, S. Nusinowitz, and J. R. Heckenlively. Cone photoreceptor function loss-3, a novel mouse model of achromatopsia due to a mutation in gnat2. *Invest Ophthalmol Vis Sci*, 47(11): 5017–21, 2006. ISSN 0146-0404 (Print) 0146-0404 (Linking). doi: 10.1167/iovs.05-1468.
16. PD Calvert, NV Krasnoperova, AL Lyubarsky, T Isayama, M Nicolo, B Kosaras, G Wong, KS Gannon, RF Margolskee, and RL Sidman. Phototransduction in transgenic mice after targeted deletion of the rod transducin β-subunit. *Proceedings of the National Academy of Sciences*, 97(25):13913–13918, 2000. ISSN 0027-8424.
17. Mehdi Azimipour, Denise Valente, Kari V. Vienola, John S. Werner, Robert J. Zawadzki, and Ravi S. Jonnal. Optoretinogram: optical measurement of human cone and rod photoreceptor responses to light. *Optics Letters*, 45(17):4658–4661, 2020. doi: 10.1364/OL.398868.
18. VJ Srinivasan, Y Chen, JS Duker, and JG Fujimoto. In vivo functional imaging of intrinsic scattering changes in the human retina with high-speed ultrahigh resolution oct. *Optics express*, 17(5):3861–3877, 2009. ISSN 1094-4087.
19. T. H. Kim, B. Wang, Y. Lu, T. Son, and X. Yao. Functional optical coherence tomography enables in vivo optoretinography of photoreceptor dysfunction due to retinal degeneration. *Biomed Opt Express*, 11(9):5306–5320, 2020. ISSN 2156-7085 (Print) 2156-7085 (Electronic) 2156-7085 (Linking). doi: 10.1364/BOE.399334.
20. Ewelina Pijewska, Pengfei Zhang, Michał Meina, Ratheesh K. Meleppat, Maciej Szkulmowski, and Robert J. Zawadzki. Extraction of phase-based optoretinograms (org) from serial b-scans acquired over tens of seconds by mouse retinal raster scanning oct system. *Biomedical Optics Express*, 12:7849, 2021. doi: 10.1364/boe.439900.
21. Xiaoyun Jiang, Teng Liu, Vimal Prabhu Pandiyan, Emily Slezak, and Ramkumar Sabesan. Coarse-scale optoretinography (coorg) with extended field-of-view for normative characterization. *Biomedical Optics Express*, 13(11):5989–6002, 2022. doi: 10.1364/BOE.473475.
22. Kari V Vienola, Denise Valente, Robert J Zawadzki, and Ravi S Jonnal. Velocity-based optoretinography for clinical applications. *Optica*, 9(10):1100–1108, 2022. ISSN 2334-2536.
23. Huakun Li, Bingyao Tan, Vimal Prabhu Pandiyan, Veluchamy Amutha Barathi, Ramkumar Sabesan, Leopold Schmetterer, and Tong Ling. Shot-noise limited phase-sensitive imaging of moving samples by phase-restoring subpixel motion correction in fourier-domain optical coherence tomography. *bioRxiv*, 2022.
24. Joe H. Ward. Hierarchical grouping to optimize an objective function. *Journal of the American Statistical Association*, 58(301):236–244, 1963. ISSN 0162-1459. doi: 10.1080/01621459.1963.10500845. doi: 10.1080/01621459.1963.10500845.
25. K. W. Yau and R. C. Hardie. Phototransduction motifs and variations. *Cell*, 139(2):246–64, 2009. ISSN 1097-4172 (Electronic) 0092-8674 (Linking). doi: 10.1016/j.cell.2009.09.029.
26. V. Y. Arshavsky, T. D. Lamb, and Jr. Pugh, E. N. G proteins and phototransduction. *Annu Rev Physiol*, 64:153–87, 2002. ISSN 0066-4278 (Print) 0066-4278 (Linking). doi: 10.1146/annurev.physiol.64.082701.102229.
27. Alfredo Dubra, Yusufu Sulai, Jennifer L Norris, Robert F Cooper, Adam M Dubis, David R Williams, and Joseph Carroll. Noninvasive imaging of the human rod photoreceptor mosaic using a confocal adaptive optics scanning ophthalmoscope. *Biomedical optics express*, 2 (7):1864–1876, 2011. ISSN 2156-7085.
28. Nathan Doble, Stacey S Choi, Johanan L Codona, Julian Christou, Jay M Enoch, and David R Williams. In vivo imaging of the human rod photoreceptor mosaic. *Optics letters*, 36(1):31–33, 2011. ISSN 1539-4794.
29. F. Naarendorp, T. M. Esdaille, S. M. Banden, J. Andrews-Labenski, O. P. Gross, and Jr. Pugh, E. N. Dark light, rod saturation, and the absolute and incremental sensitivity of mouse cone vision. *J Neurosci*, 30(37):12495–507, 2010. ISSN 1529-2401 (Electronic) 0270-6474 (Print) 0270-6474 (Linking). doi: 10.1523/JNEUROSCI.2186-10.2010.
30. K. P. Szatko, M. M. Korympidou, Y. Ran, P. Berens, D. Dalkara, T. Schubert, T. Euler, and K. Franke. Neural circuits in the mouse retina support color vision in the upper visual field. *Nat Commun*, 11(1):3481, 2020. ISSN 2041-1723 (Electronic) 2041-1723 (Linking). doi: 10.1038/s41467-020-17113-8.
31. Guangying Ma, Taeyoon Son, Tae-Hoon Kim, and Xincheng Yao. Functional optoretinography: concurrent oct monitoring of intrinsic signal amplitude and phase dynamics in human photoreceptors. *Biomedical Optics Express*, 12(5):2661–2669, 2021. ISSN 2156-7085.
32. Elizabeth S Russell and Seldon E Bernstein. Blood and blood formation. *Biology of the laboratory mouse*, 2:351–372, 1966.
33. Gregory M Preston, Tiziana Piazza Carroll, William B Guggino, and Peter Agre. Appearance of water channels in xenopus oocytes expressing red cell chip28 protein. *Science*, 256 (5055):385–387, 1992. ISSN 0036-8075.
34. Juan I Korenbrot, Dennis T Brown, and Richard A Cone. Membrane characteristics and osmotic behavior of isolated rod outer segments. *The Journal of Cell Biology*, 56(2):389–398, 1973. ISSN 1540-8140.
35. Bo Huang and CJ Karwoski. Light-evoked expansion of subretinal space volume in the retina of the frog. *Journal of Neuroscience*, 12(11):4243–4252, 1992. ISSN 0270-6474.
36. Jian-dong Li, Ron P Gallemore, Andrey Dmitriev, and Roy H Steinberg. Light-dependent hydration of the space surrounding photoreceptors in chick retina. *Investigative ophthalmology & visual science*, 35(6):2700–2711, 1994. ISSN 1552-5783.
37. O. Strauss. The retinal pigment epithelium in visual function. *Physiol Rev*, 85(3):845–81, 2005. ISSN 0031-9333 (Print) 0031-9333 (Linking). doi: 10.1152/physrev.00021.2004.
38. MC Campbell and A Hughes. An analytic, gradient index schematic lens and eye for the rat which predicts aberrations for finite pupils. *Vision Research*, 21:1129–1148, 1981.
39. Y. V. Wang, M. Weick, and J. B. Demb. Spectral and temporal sensitivity of cone-mediated responses in mouse retinal ganglion cells. *J Neurosci*, 31(21):7670–81, 2011. ISSN 1529-2401 (Electronic) 0270-6474 (Linking). doi: 10.1523/JNEUROSCI.0629-11.2011.
40. I Perlman. Kinetics of bleaching and regeneration of rhodopsin in abnormal (rcs) and normal albino rats in vivo. *The Journal of Physiology*, 278(1):141–159, 1978. ISSN 0022-3751. doi: https://doi.org/10.1113/jphysiol.1978.sp012297.
41. Pengfei Zhang, Mayank Goswami, Robert J. Zawadzki, and Jr Pugh, Edward N. The photosensitivity of rhodopsin bleaching and light-induced increases of fundus reflectance in mice measured in vivo with scanning laser ophthalmoscopy. *Investigative Ophthalmology & Visual Science*, 57(8):3650–3664, 2016. ISSN 1552-5783. doi: 10.1167/iovs.16-19393.
42. V. Choh, A. Gurdita, B. Tan, Y. Feng, K. Bizheva, D. L. McCulloch, and K. M. Joos. Isoflurane and ketamine:xylazine differentially affect intraocular pressure-associated scotopic threshold responses in sprague-dawley rats. *Doc Ophthalmol*, 135(2):121–132, 2017. ISSN 1573-2622 (Electronic) 0012-4486 (Print) 0012-4486 (Linking). doi: 10.1007/s10633-017-9597-7.
43. Govind Nair, Moon Kim, Tsukasa Nagaoka, Darin E Olson, Peter M Thulé, Machelle T Pardue, and Timothy Q Duong. Effects of common anesthetics on eye movement and electroretinogram. *Documenta Ophthalmologica*, 122:163–76, 2011. doi: 10.1007/s10633-011-9271-4.
44. Manuel Guizar-Sicairos, Samuel T Thurman, and James R Fienup. Efficient subpixel image registration algorithms. *Optics letters*, 33(2):156–158, 2008. ISSN 1539-4794.
45. Francesco LaRocca, Stephanie J. Chiu, Ryan P. McNabb, Anthony N. Kuo, Joseph A. Izatt, and Sina Farsiu. Robust automatic segmentation of corneal layer boundaries in sdoct images using graph theory and dynamic programming. *Biomedical Optics Express*, 2(6):1524–1538, 2011. doi: 10.1364/boe.2.001524.
46. Frédéric Ros and Serge Guillaume. A hierarchical clustering algorithm and an improvement of the single linkage criterion to deal with noise. *Expert Systems with Applications*, 128: 96–108, 2019. ISSN 0957-4174. doi: https://doi.org/10.1016/j.eswa.2019.03.031.
47. Edwin M Knox and Raymond T Ng. Algorithms for mining distancebased outliers in large datasets. In *Proceedings of the international conference on very large data bases*, pages 392–403. Citeseer, 1998.
48. Emrah Hancer and Dervis Karaboga. A comprehensive survey of traditional, merge-split and evolutionary approaches proposed for determination of cluster number. *Swarm and Evolutionary Computation*, 32:49–67, 2017. ISSN 2210-6502. doi: https://doi.org/10.1016/j.swevo.2016.06.004.
49. K. Unglert, V. Radić, and A. M. Jellinek. Principal component analysis vs. self-organizing maps combined with hierarchical clustering for pattern recognition in volcano seismic spectra. *Journal of Volcanology and Geothermal Research*, 320:58–74, 2016. ISSN 0377-0273. doi: https://doi.org/10.1016/j.jvolgeores.2016.04.014.


DRAFT